Acoustic Field Around a Transonic Cavity Flow

G.J.M. Loupy[1] , G.N. Barakos[2]

CFD Laboratory, University of Glasgow, Glasgow, G12 8QQ, UK
and A. Kusyumov[3]
Kazan State Technical University, 10 K. Marx Street, Kazan 420111, Russia

Abstract

This paper describes new techniques for analysing cavity flows. The beamforming method is used to estimate the pressure fluctuations inside a resonant transonic cavity, highlighting the localisation of the sources of noise. The method produces insightful results and only requires the use of an acoustic array and a mean flow-field. The technique models the noise propagation in a simple and efficient way, applicable for wind tunnel test. In addition, this paper discusses the generation of the cavity tones. CFD results are analysed using a superposition of reflected acoustic waves driven by the cavity flow. This analysis shows that the time averaged flow-field drives the frequencies of the tones, while the flow-field fluctuations drive their amplitude. In addition, the tonal dynamics of the cavity flow are represented by a simple model with standing wave oscillations and their modulation. This work is complementary to the well established Rossiter cavity model.

---

[1]PhD Student. g.loupy.1@research.gla.ac.uk

[2]Professor, MAIAA, MRAeS, MAHS. george.barakos@glasgow.ac.uk, corresponding author

[3]Professor. postbox7@mail.ru

Latin

a	Wavelet dilatation or scale (1/s)
A_f	Pressure wave amplitude (Pa)
A_t	Absorption coefficient(-)
b	Wavelet translation parameter (s)
c	Sound speed (m/s)
$\mathbf{c_w}$	Wave velocity vector (m/s)
C_P	Pressure coefficient (-)
c_j^{n-}, c_j^{n+}	Upstream, and downstream wave speed at point j and time n (m/s)
D	Cavity depth (m)
$e(\omega)$	Steering vector
f	Frequency (Hz)
f_N	Maximum pressure wave frequency (Hz)
f_m	Frequency of Rossiter mode m (Hz)
i, j, k	Cell index (-)
k	Specific turbulent kinetic energy (m^2/s^2)
L	Cavity length (m)
m	Rossiter mode number (-)
M_∞	Free-stream Mach number (-)
N_p	Number of points along the cavity length (-)
N_r	Number of reflections (-)
P	Pressure (Pa)
$P_{i,j}^n$	i-th wave reflection amplitude at point j, and time n (Pa)
P_{ref}	International standard minimum audible sound $(2.10^{-5}Pa)$
R	Cross spectral matrix
$\mathbf{R}_{i,j,k}$	Flux residual vector
Re_L	Reynolds number based on cavity length (-)
R_w	Reflection coefficient (-)
u, v, w	Velocity components (m/s)
$\mathbf{U}$	Velocity vector (m/s)
U_∞	Free-stream Velocity (m/s)
u_j^n	Axial flow-field velocity at point j and time n (m/s)
$V_{i,j,k}$	Volume of the cell i,j,k (m^3)
W	Cavity width (m)
W_Ψ^y	Wavelet transform
$\mathbf{w}_{i,j,k}$	Vector of conservative variables
$\mathbf{x}$	Position vector

1

Latin

y_m	Signal of microphone m
X, Y, Z	Cartesian coordinates (m)
$Z(\omega)$	Beamformer output
$Z_{steel}, Z_{air} = \rho c$	Acoustic impedance ($kg/m^2 s$)

Greek

α	Rossiter Phase shift (-)
Δf_{ref}	Reference frequency (Hz)
Δm	Beamforming time delay (s)
κ_ν	Rossiter convection velocity coefficient (-)
γ	Ratio of specific heats of air (-)
ω	Specific turbulence dissipation rate (1/s)
ω_0	Pulsation ($2\pi f$) (1/s)
$\Psi(t)$	Mother wavelet (-)
ρ	Density (kg/m^3)

Acronyms

ALE	Arbitrary Lagrangian-Eulerian
$BILU$	Block Incomplete Lower-Upper
$BISPL$	Banded Integrated Sound Pressure Level
BIW	Banded Integrated Wavelet
CFD	Computational Fluid Dynamics
CFL	CourantFriedrichsLewy
FFT	Fast Fourier Transforms
HMB	Helicopter Multi-Block
MEM	Maximum Entropy Method
$MUSCL$	Monotone Upwind Schemes for Scalar Conservation Laws
$MUSIC$	MUltiple SIgnal Classification
$OASPL$	Overall Sound-Pressure Level
PIV	Particle Image Velocimetry
PSD	Power Spectral Density
$RK4$	Runge-Kutta method 4th order
SAS	Scale Adaptive Simulation
SPL	Sound-Pressure Level
$UCAV$	Unmanned Combat Air Vehicle
$URANS$	Unsteady Reynolds-Averaged Navier-Stokes

1   Introduction

Weapon bays improve the stealth of military aircraft and Unmanned Combat Air Vehicles (UCAVs). However, exposed cavities generate strong structure loading, due to resonant pressure fluctuations inside the bay. The cavity flow acoustics comprises broadband and tonal noise, called Rossiter modes [1], generated by a complex interaction between the shear layer, and reflected acoustic waves between the cavity walls [2]. The acoustic field around ideal cavity flow is well studied as shown in Lawson and Barakos [3]. Nevertheless, the accurate prediction of the cavity modes can only be achieved by experiments or CFD which are expensive and time consuming.

Using experimental, and CFD results, numerous authors tried to model the tone generation mechanism in cavity flows. Tam *et al.*[4] proposed to take into account flow characteristics including the shear layer thickness, and the a small number of acoustics reflections, agreeing well with the experimental frequencies. Handa *et al.*[5] developed a model for the acoustic feedback mechanism based on superposition of two reflected waves. Their results predicted well the tonal frequencies of deep cavity flows. The model of Alvarez*et al.*[6] based on the scattering process at each cavity ends is the only one predicting the existence of the cavity modes. Nevertheless, the cavity dynamics is not predicted by existing works, and the understanding of cavity flow did not really changed since Rossiter's [1] study. His theoretical model gives the modal frequencies, based on the interaction between an assumed periodic shear layer vortex shedding, and the acoustic waves travelling along the bay. The semi-empirical formula available for the estimation of the tonal frequencies, as modified by Heller [7] is:

$$f_m = \frac{U_\infty}{L} \left[\frac{m - \alpha}{M_\infty \left(1 + \left(\frac{\gamma-1}{2}\right) M_\infty^2\right)^{-1/2} + 1/\kappa_\nu} \right] \tag{1}$$

where f_m is the frequency of mode m, U_∞ is the free-stream velocity, M_∞ is the free-stream Mach number, L is the cavity length, γ is the ratio of specific heats of the employed gas, α represents a phase shift, and κ_ν is the convection velocity coefficient of the vortices in the shear layer. These empirical constants have the values 1.4, 0.25 and 0.57 respectively for the present study. Experimental data [2, 8] show that Rossiter's formula can be valid even if κ_ν is different from the value found by Rossiter. In addition, the lack of prediction of the modal amplitude, and the prediction of too many

modes [3], show that a part the cavity physics may be missing from existing model.

The origin of the unsteady pressure field components including standing waves, mode switching, and modulation of the tonal amplitude [9] is not well understood. The combination of those pressure fluctuations leads to aperiodic loading, driving store trajectory variability. Joint time-frequency methods like the wavelet transform [8] are able to dissect the temporal behaviour of the tones, and proved that linear coupling between modes [9] is negligible. In this work, this method is extended to perform a joint space-time-frequency analysis of the pressure field, to validate the flow dynamics of CFD and modelling.

To improve the understanding of cavity flows, recent works applied novel experimental techniques for pressure measurement, like the sensitive pressure paint [10] highlighting the pressure fluctuations over all the surfaces. Nevertheless, the pressure fluctuations at the shear layer, where the sound pressure levels peak, are still difficult to measure without intrusive techniques. This work assesses the beamforming technique for cavity flow, which may help researchers to capture the acoustic field far from the walls using a limited number of probes.

This paper is organised as follows. First, the CFD methodology, and the post-processing techniques are presented. After, Scale Adaptive Simulation is validated using PSD, OASPL, and joint time-frequency analysis. Then, the mean CFD flow is employed with the beamforming technique to assess the influence of the microphone array position, density, and shape on the noise field reconstruction. Finally, a cavity flow model is built and compared to experimental data. Novel ideas and insight on the tone generation are drawn from the obtained results.

2 CFD Methodology

The Helicopter Multi-Block (HMB3) [11] code is used for the present work. HMB3 solves the Unsteady Reynolds (Favre) Averaged Navier-Stokes (URANS) equations in integral form using the arbitrary Lagrangian-Eulerian (ALE) formulation, first proposed by Hirt *et al.* [12], for time-dependent domains, which may include moving boundaries. The Navier-Stokes equations are discretised using a cell-centred finite volume approach on a multi-block grid. The spatial discretisation of these equations leads to a set of ordinary differ-

4

ential equations in time,

$$\frac{d}{dt}(\mathbf{w}_{i,j,k}V_{i,j,k}) = -\mathbf{R}_{i,j,k}(\mathbf{w}) \tag{2}$$

where i, j, k represent the cell index, $\mathbf{w}$ and $\mathbf{R}$ are the vector of conservative variables and flux residual respectively and $V_{i,j,k}$ is the volume of the cell i, j, k. To evaluate the convective fluxes, the Osher [13] and Roe [14] approximate Riemann solvers are used and the viscous terms are discretised using a second order central differencing spatial discretisation. The Monotone Upstream-centred Schemes for Conservation Laws (MUSCL) of Leer [15], is used to provide third order accuracy in space. The HMB3 solver uses the Albada limiter [16] that is activated in regions where large gradients are encountered due to shock waves, avoiding non-physical, spurious oscillations. An implicit dual-time stepping method is employed to performed the temporal integration, where the solution is marching in pseudo-time iterations to achieve fast convergence, which is solved using a first-order backward difference. The linearised system of equations is solved using the Generalised Conjugate Gradient method with a Block Incomplete Lower-Upper (BILU) factorisation as a pre-conditioner [17]. The implicit scheme requires a small CFL at the early iterations or some explicit iteration using the forward Euler or four stage Runge-Kutta (RK4) methods [18]. Multi-block structured meshes are used with HMB3, which allow an easy sharing of the calculation load for parallel execution. The structured multi-block hexa meshes are generated using the ICEM-Hexa™tool of ANSYS. An overset grid method is available in HMB3 [19], to allow relative motion between mesh components. The chimera method is based on composite grids, consisting of independently generated, overlapping non-matching sub-domains. Each of these sub-domains are referred to as a Level and are sorted hierarchically, with higher levels having priority. The exchange of information between sub-domains is achieved through interpolation and by following the level hierarchy. The work presented in this paper uses Scale-Adaptive Simulation (SAS) [20, 21]. SAS was successfully used for cavity flows, being an order of magnitude faster than DES and LES [22].

3 Flow Analysis Methods

This section presents the techniques used to analyse the unsteady flow data. CFD flow-field files are written at specific instances in time, and flow "probes" at specific mesh points are sampled at every time step.

3.1 Pressure Signals

The Power Spectral Density (PSD), Overall Sound-Pressure Level (OASPL) and Band-Integrated Sound-Pressure Level (BISPL) are the basis of comparison for numerical unsteady pressure data. The PSD is used to study the frequency content of a signal at a given location and is based upon the unsteady pressure P', where $P' = P - \overline{P}$. The PSD was calculated using the Burg Estimator [23] (also known as Maximum Entropy Methods or MEM) as it produces better resolved peaks for short signals than traditional Fast Fourier Transforms (FFT) [24]. For a description of the PSD in terms of decibels (dB), the natural definition is that of the Sound-Pressure spectrum Level (SPL) [25]:

$$SPL(f) = 10 \ \text{LOG}_{10} \left[\frac{PSD(f) \ \Delta f_{ref}}{P_{ref}^2} \right] \tag{3}$$

where Δf_{ref} is a reference frequency, usually set to 1 Hz and P_{ref} is the international standard for the minimum audible sound, which has the value of 2×10^{-5} Pa [25].

The variation in pressure levels along the cavity floor was studied using the Root-Mean-Square (RMS) of the unsteady pressure, P'_{rms}. Although P'_{rms} is measured in Pascal (or any other unit of pressure), it is customary in cavity flow studies to report it as the Overall Sound-Pressure Level(OASPL) [25]:

$$OASPL = 20 \ \text{LOG}_{10} \left[\frac{P'_{rms}}{p_{ref}} \right] \tag{4}$$

which has the units of decibels. BISPL plots show the energy content within a particular frequency range and are calculated using the following equation:

$$BISPL = 20 \ \text{LOG}_{10} \left[\left(\int_{f_1}^{f_2} PSD(f) \right)^{1/2} \cdot \frac{1}{P_{ref}} \right] \tag{5}$$

6

where f_1 and f_2 are the lower and upper limits of the desired frequency range. For cavity flow studies, the BISPL plots are centred around the first four Rossiter Modes.

3.2   Time Frequency Analysis - Morlet Wavelet Method

The cavity flow is highly unsteady, and its dynamics must be understood to gain insight in its physics. The continuous Morlet wavelet transform is a method for time-frequency analysis [26], that reveals the temporal fluctuations of the different frequencies present in the flow. The wavelet transform $W_\Psi^y(f,t)$ is a convolution of the signal $s(t)' = s(t) - \overline{s}$ with a scaled mother wavelet $\Psi(t)$ conserving the sign of the signals in time and frequency:

$$W_\Psi^y(a,b) = \frac{1}{\sqrt{c_\Psi\, |a|}} \int_{-\infty}^{\infty} s'(t)\Psi\left(\frac{t-b}{a}\right) dt.$$
(6)

In the above equation, a is called the dilatation or the scale, b the translation parameter, $c_\Psi = \sqrt{\pi/\beta}$ and $\beta = \omega_0^2$. The dilatation a is related to the frequency f of the wavelet, the translation parameter b is related to the time shift t of the wavelet. The mother, or Gabor wavelet $\Psi(t)$ is given by :

$$\Psi(t) = e^{\frac{-\beta t^2}{2}} e^{j\omega t}$$
(7)

Band Integrated Wavelets (BIW) plots show the energy content within a particular frequency range and is calculated using the following equation:

$$BIW(t) = \int_{f_1}^{f_2} W_\Psi^y(f,t)^2$$
(8)

where f_1 and f_2 are the lower and upper limits of the desired frequency range. The wavelets in decibel are given by:

$$W_{dB}(f,t) = 20\ \mathrm{LOG}_{10}\left[\frac{W_\Psi^y(f,t)^2}{p_{ref}}\right]$$
(9)

with p_{ref} the international standard for the minimum audible sound, which has the value of 2.10^{-5} Pa [25].

The wavelet envelope BIW_{dB} is the amplitude of the frequency in time, and is determined using the maximum of the absolute value of the wavelet transform $W_\Psi^y(f,t)$ over windows equal to half of a period of the frequency.

3.3 Noise Source Analysis: Beamforming

Cavity flows are characterised by large level of noise. Typically, single microphone measurements, cannot distinguish between pressure contributions from different sources. Measurements from an acoustic array, instead, allow to determine the location of the acoustic sources, by means of a combination of the individual microphone signals [27]. This technique is useful for wind tunnel testing as it is not possible to measure the pressure at every point of the flow-field. Nevertheless, this technique has not been used for cavity flows, to date. The output of the beamforming algorithm is a noise map, which shows the power detected at each scanned grid point in terms of decibels below the peak power. Given an array with M microphones, the waveform output of the m-th sensor will differ from the reference sensor of the array by a time delay. Therefore, the beamformer waveform output $z(t)$ can be written as the weighted sum of the sensor waveform outputs:

$$z(t) \triangleq \sum_{m=0}^{M-1} y_m(t - \Delta_m),$$ (10)

where $y_m(t)$ is the signal of the m-th microphone of the array, and Δ_m the time delay. The time delay is defined as $\Delta_m \triangleq \frac{r_m - r_0}{c}$, where r_m is the distance from the assumed source position $\overrightarrow{x_0}$ and the m-th sensor and c is the speed of sound. The conventional beamforming computes the output using the frequency representation of $z(t)$ obtained by a Fourier transformation of the microphones signals.

$$Z(\omega) = \mathcal{F}\left\{\sum_{m=0}^{M-1} y_m(t - \Delta_m)\right\} = \sum_{m=0}^{M-1} Y_\omega e^{-j\Delta_m \omega}.$$ (11)

If we define as $Y(\omega_k)$ an $M \times 1$ vector of complex numbers containing the signal amplitude and phase, at a frequency ω_k, for each array sensor, and $e(\omega_k)$ as the *steering* $M \times 1$ vector containing the weight and phase delay information of the sensors for an assumed source location $\overrightarrow{x_0}$, then we can write

$$Z(\omega_k) = e(\omega_k)^\dagger Y(\omega_k) = e_k^\dagger Y_k,$$ (12)

where k is the k-th frequency bin we can detect in the digital signal processing and † the Hermitian transpose operator.

The power detected at the k-th frequency bin is defined as

$$P_k \triangleq \mid Z_k \mid^2 = Z_k Z_k^*.$$ (13)

8

Therefore, using the definitions introduced before:

$$P_k = e_k^\dagger \left(Y_k Y_k^\dagger \right) e_k = e_k^\dagger R e_k \tag{14}$$

where R is the cross spectral matrix. The results are characterised by the main lobe width, that has to be as narrow as possible, and side lobes at relatively lower levels that have to be as low as possible. This paper uses the Multiple Signal Classification (MUSIC) Algorithm to compute P_k [28]. This is known to improve the response characteristics than linear techniques.

3.3.1 Noise Propagation Model

A sound wave around a transonic cavity flow travels in a non-uniform flow-field and has a speed close to the free-stream velocity. Consequently, the path to go from a source to a microphone is not a straight line. To use the beamforming algorithm, the distance between a source and a microphone has to take into account the path of the noise, and the noise propagation model is defined as follow. It is assumed that the noise sources radiate uniformly around them. The sound wave emitted in the direction of the microphone with an velocity V_0 of norm equal to the speed of sound c is considered. The trajectory of the wave is computed taking into account the transport by the flow-field. The length of the trajectory d_{travel} is the distance to go from the source to the microphone, and c_{travel} the mean velocity along the trajectory. Then, the initial velocity of the sound wave V_0 is changed taking into account the offset distance d_{off} between the trajectory and the microphone:

$$V_0 = V_0 - d_{off} \frac{c_{travel}}{d_{travel}} \tag{15}$$

The initial velocity is normalised to a norm c and a new wave is launched with the new initial velocity. This process is repeated until a trajectory reaches the microphone. Furthermore, the wave does not have a constant velocity along the trajectory, therefore, the equivalent distance r_m along the trajectory at a constant velocity c is given by:

$$r_m = d_{travel} \frac{c}{c_{travel}} \tag{16}$$

This beamforming algorithm has been validated on a simple case of two speakers in front of an array of 40 microphones without free-stream. The
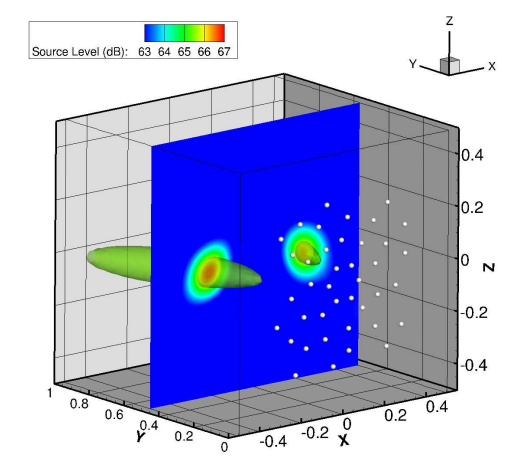
Figure 1: Validation of the beamforming analysis.

microphone signals were sampled at 48kHz and recorded during 3 seconds. Figure 1 shows the microphone array in white dots and the beamforming result for the frequency of 1800Hz generated by the speakers. The space is scanned for sources in a cube of 1m side around the speakers. The speaker's positions are correctly found at 0.51m in front of the microphone array. However, the lobes shown in the figure 1 are very large in the sound propagation direction. More microphones distributed along the sound propagation direction are needed to reduce the lobe size.

4   Geometric and Computational Model

The simulations were carried out for the M219 cavity [29]. M219 has a length to depth ratio of 5, a width to depth ratio of 1, and a length of 0.51m. Experiments were carried out by Nightingale *et al.*[29] at a Mach Number of 0.85, and a Reynolds Re_L, based on the cavity length, of 6.5 million. Two cavities are computed, one has two doors attached at its sides at an angle of 90 degrees (Figure 2), and the other one has no doors. Experimental data were obtained using Kulite^{TM} pressure transducers at the cavity ceiling. Three grid densities of 13, 22 and 34 million points are compared to the experimental data for the cavity with doors. The computational grids computed with a dimensionless time-step of 0.01 are presented in table 1.

This paper uses different microphone arrays to show the effect of their

position, density, and shape with the beamforming technique (Table 2). Two array shapes that give accurate source identification for far-field noise are tested [30]: the multi-spiral design (Figure 3a), composed of spirals equally rotated about the origin, and the Dougherty log-spiral design (Figure 3b), built with microphones equally spaced along a logarithmic spiral. The multi-

Cavity	Door Angle (deg)	Grid size (10^6 cells)	Cavity Travel Times
M219	90	13.2	25
M219	90	22.3	25
M219	90	33.9	30
M219	No doors	23.0	30

Table 1: Details of the configurations computed with SAS.

(a) Bottom view

(b) Downstream view

(c) Surface mesh - Fine
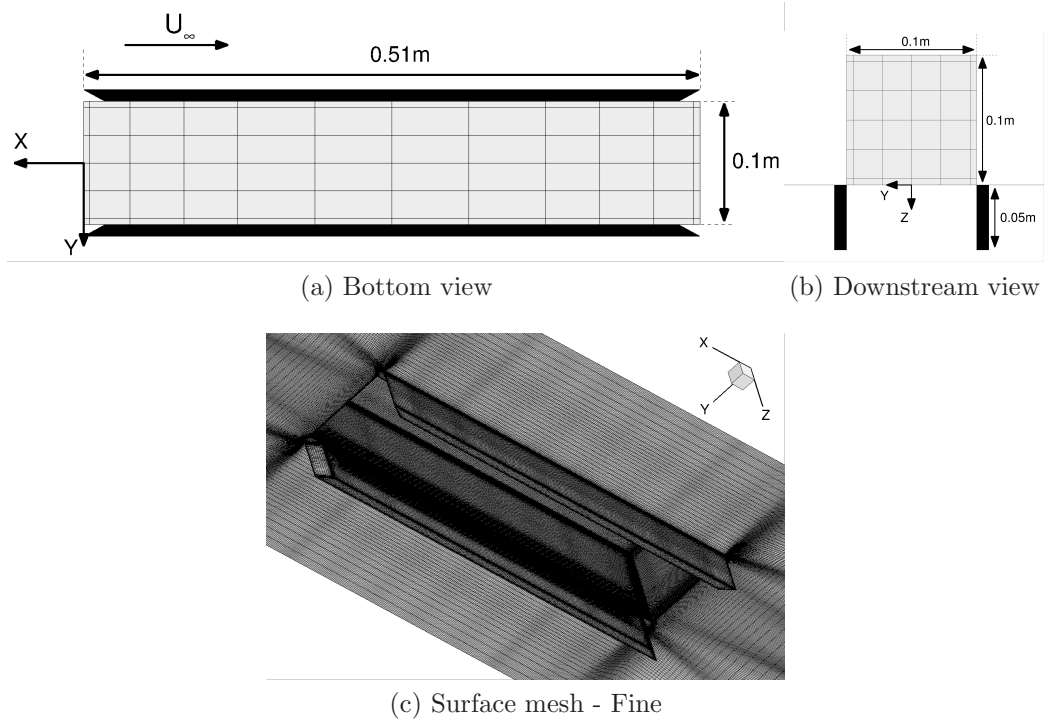
Figure 2: Schematic view of the M219 cavity with doors. Cavity in light grey and doors in black.

spiral design is tested with 31, 61, and 101 microphones, and for different vertical positions. The arrays are centred on the aft wall of the cavity to take into account the flow-field that moves the focus point of the array upstream. Those arrays could be fitted in the DERA Bedford wind-tunnel where the experiments were performed.

Shape	Z/L	Nb microphone
Multispiral	0.6	31
Multispiral	0.9	31
Multispiral	1.2	31
Multispiral	1.5	31
Multispiral	1.5	61
Multispiral	1.5	101
Dougherty	1.5	31

Table 2: Details of the microphone arrays

(a) Multi-spiral design   (b) Dougherty Design
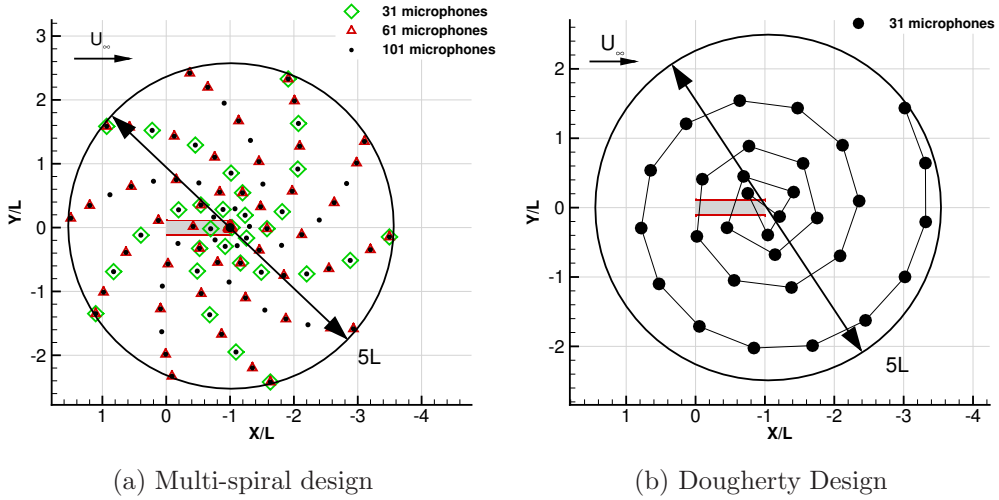
Figure 3: Schematic view of the microphone arrays.

No wind tunnel data is available to validate the beamforming algorithm with the microphone arrays arranged around a cavity. To perform a validation, three noise sources of equal intensity are placed along the shear layer,

12

at the front, the middle, and the aft of the cavity. The sources radiate a noise at 400Hz that corresponds to the dominant cavity mode of the present case. The signal received by the microphones are computed using the propagation model described in section 3.3.1, and the mean flow computed with CFD. Here the multi-spiral and the Dougherty arrays of 31 probes placed at Z/L=1.5 are employed. Finally, beamforming is applied with the simulated microphone signals. The reconstructions are shown figure 4, with the sources marked with black crosses. Both arrays localise all noise sources, surrounded by lobes spreading along the vertical axis. However, the Dougherty design is slightly worst, with larger lobes.

(a) Multi-spiral Design   (b) Dougherty Design
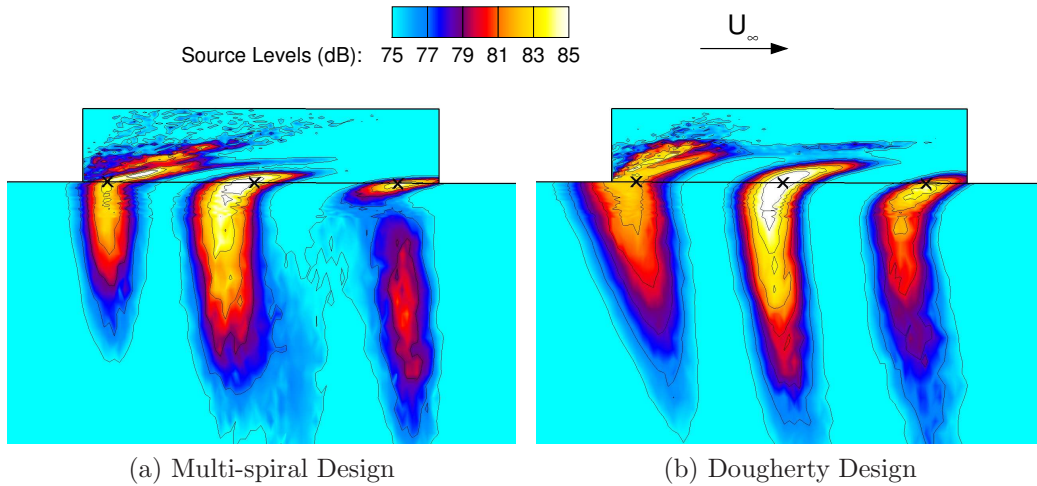
Figure 4: Reconstruction of three noise sources at shear layer.

5   Validation of the CFD Method

5.1   Averaged Pressure Validation

First, the flow over the M219 cavity with door is validated. Figure 5 shows the SPL comparison between CFD and experiments at three points at 5%L, 45%L, and 95%L on the ceiling mid-span. Since the CFD simulations are run for a typical length of 25 travel times, and the experimental data span 1900 travel times, the comparison is carried out as follows. The experiment is divided in windows of 25 travel time, and the result leads to the envelope

shown with the SPL. The SPL shows better agreement with the test data when the fine grid is used, capturing both the tones and the broadband noise.

The time averaged C_P (Figure 6a) along the ceiling mid-span, shows the grid convergence, with negligible changes between the different grid densities. The OASPL, on figure 6b is shown with error bars, computed as for figure 5. The second Rossiter mode is dominant, with a W shape of the OASPL, as captured by the CFD and the experiments [31].

The CFD is compared with the experiments of the cavity without doors on figure 7. Overall, the CFD captured well the noise field in terms of SPL and OASPL. The OASPL is overestimated by the CFD all along the

(a) X/L=0.05   (b) X/L=0.45   (c) X/L=0.95
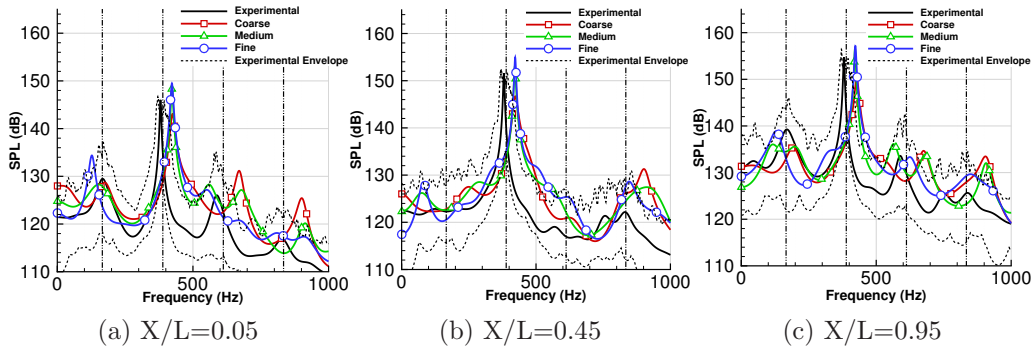
Figure 5: M219 cavity with door SPL along the ceiling mid-span. Vertical black lines are the Rossiter modes.

(a) Mean Cp   (b) OASPL
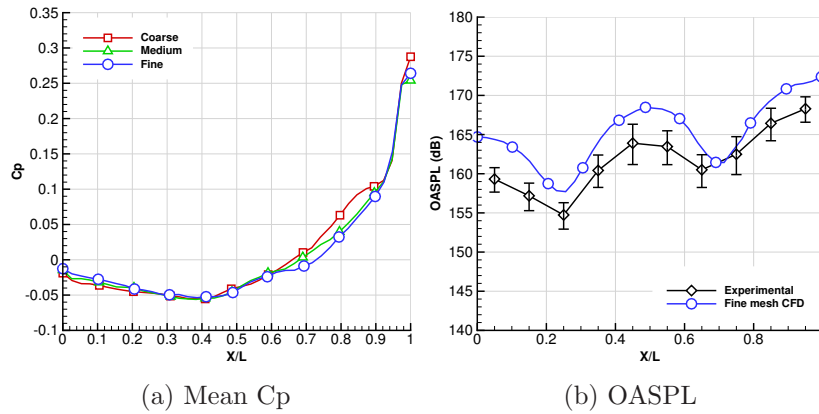
Figure 6: OASPL, and mean C_P along the M219 cavity ceiling mid-span.

14

cavity length. A large number of simulations performed with various models [32, 33, 34] have shown a similar overestimation that may also be due to experimental errors, as well as limitations of the SAS and DES approaches. The time averaged stream-wise velocity is compared in figure 7c between CFD and PIV experiments [35]. The CFD results agree well with the experiments, showing the development of the shear layer along the cavity length.
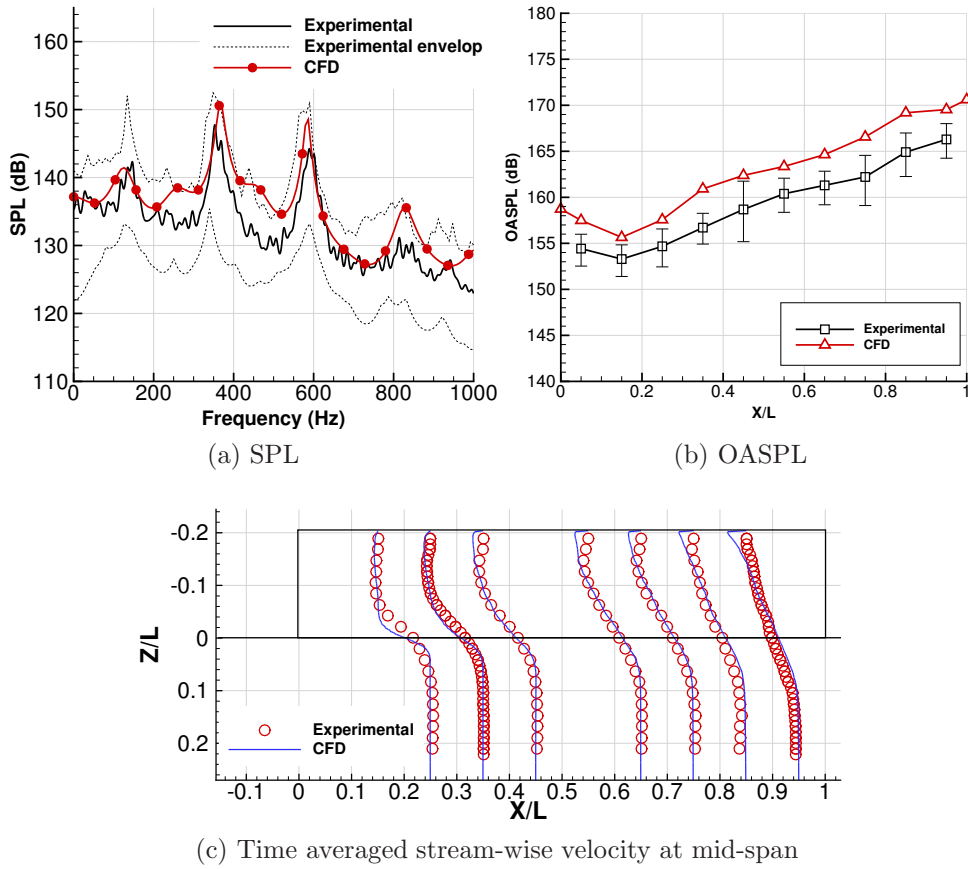

(a) SPL

(b) OASPL

(c) Time averaged stream-wise velocity at mid-span

Figure 7: Validation of the M219 cavity without doors

5.2 Spatio-Temporal Pressure Validation

The wavelet transform is used to perform spatio-temporal validation of the CFD signals. The pressure probes are analysed, and the Banded Integral

15

Wavelet (BIW) is represented on figure 8 for 25 travel times, along the ceiling centre line. The scalogram is integrated in windows of 20Hz centred on the first, and second cavity modes. There is a fair agreement of the CFD with the experiments, showing standing waves oscillations, characterised by nodes (minima of amplitude), and antinodes (maxima of amplitude). Furthermore, there is phase opposition between neighbours antinodes. This behavior is also seen for higher frequency modes, as also pointed out by Rossiter [1] in

(a) Experimental - Mode 1 (b) Experimental - Mode 2

(c) CFD - Mode 1 (d) CFD - Mode 2
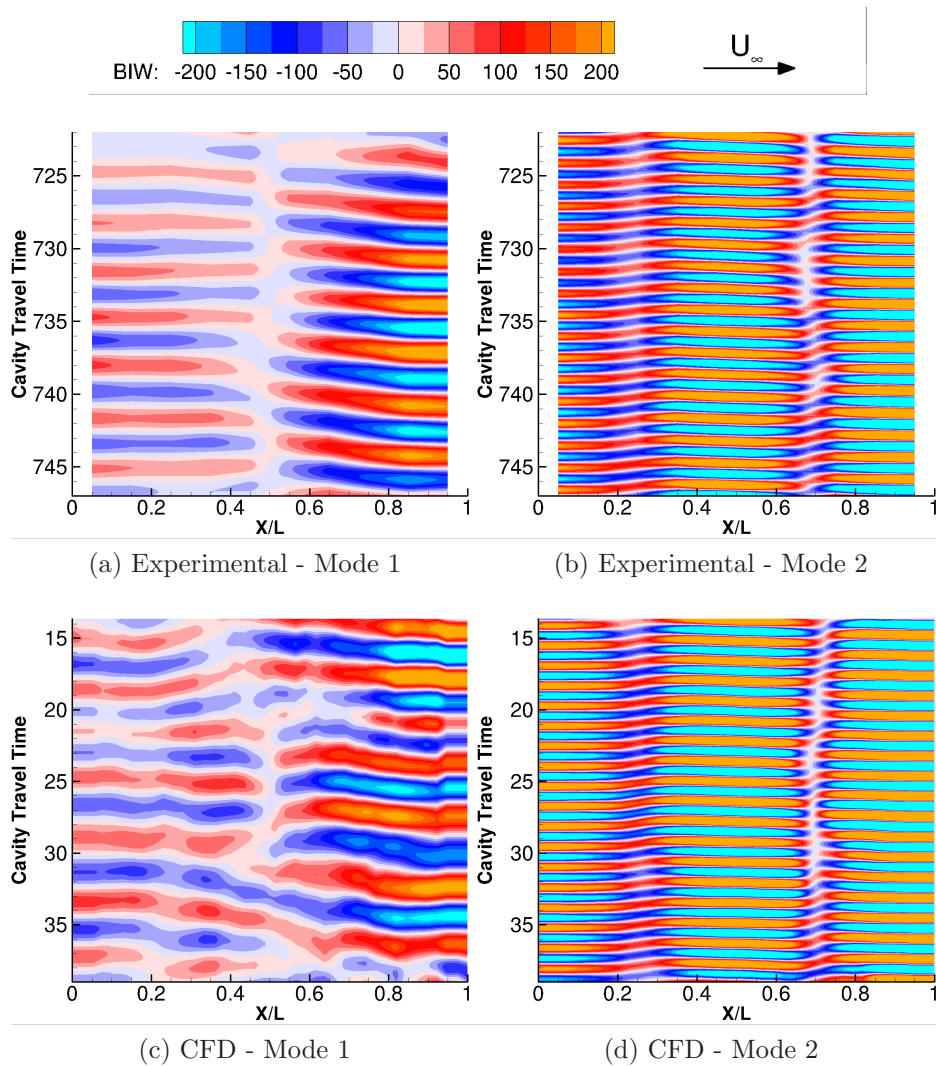
Figure 8: BIW at the cavity ceiling centre-line for modes 1 and 2.

16

the construction of his model for the flow flow dynamics and acoustics.

The BIW envelope is shown figure 9. The CFD signal agrees with the experiments showing the characteristic shape of the first mode, with two antinodes at the front, and the aft wall. The second mode shows the W shape seen on the OASPL. The modal amplitude is not constant over time, with global fluctuations all along the cavity. For example, the second CFD mode (Figure 9d) shows three maxima at travel times of 19, 27, and 35.
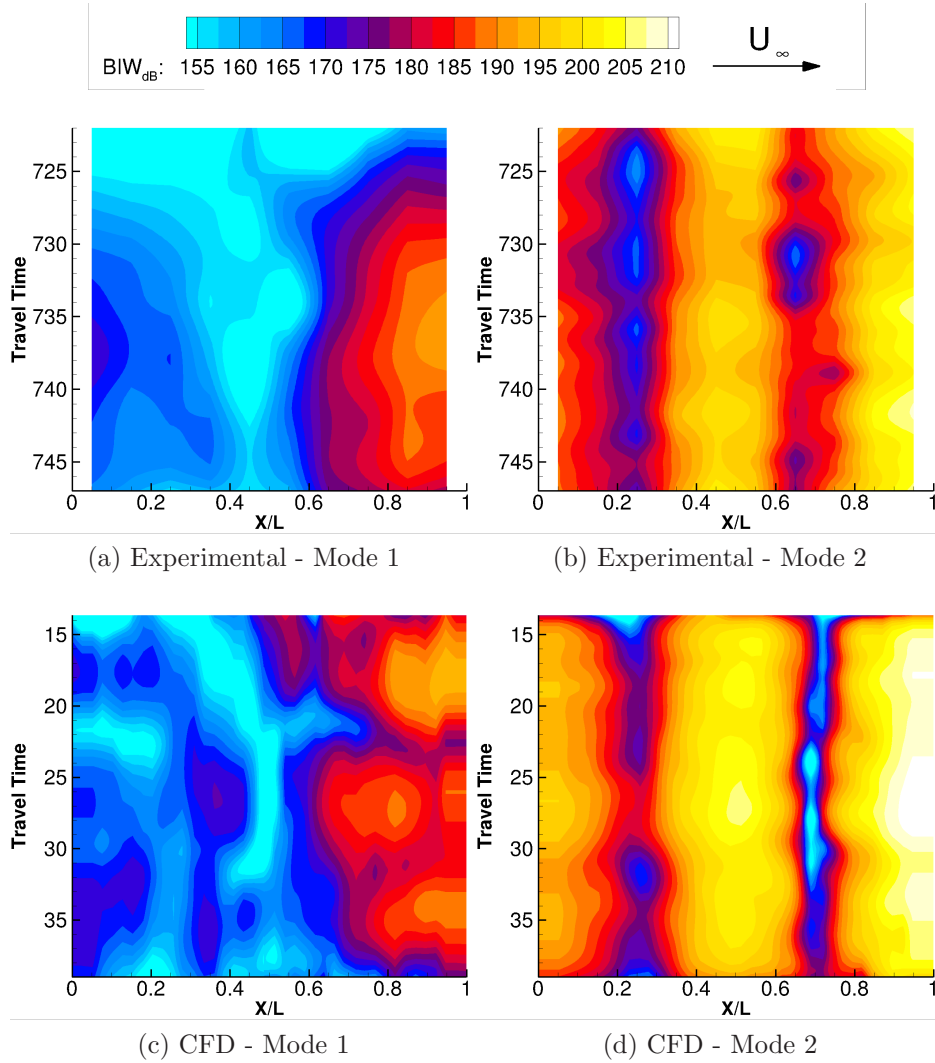

(a) Experimental - Mode 1   (b) Experimental - Mode 2

(c) CFD - Mode 1   (d) CFD - Mode 2

Figure 9: BIW amplitude at the cavity ceiling centre-line for modes 1 and 2.

Those amplitude oscillations, denoted as mode amplitude modulation, were also described in experimental works [9]. The SAS turbulence model successfully captured the transonic cavity flow pressure field for both, averaged and spatio-temporal components.
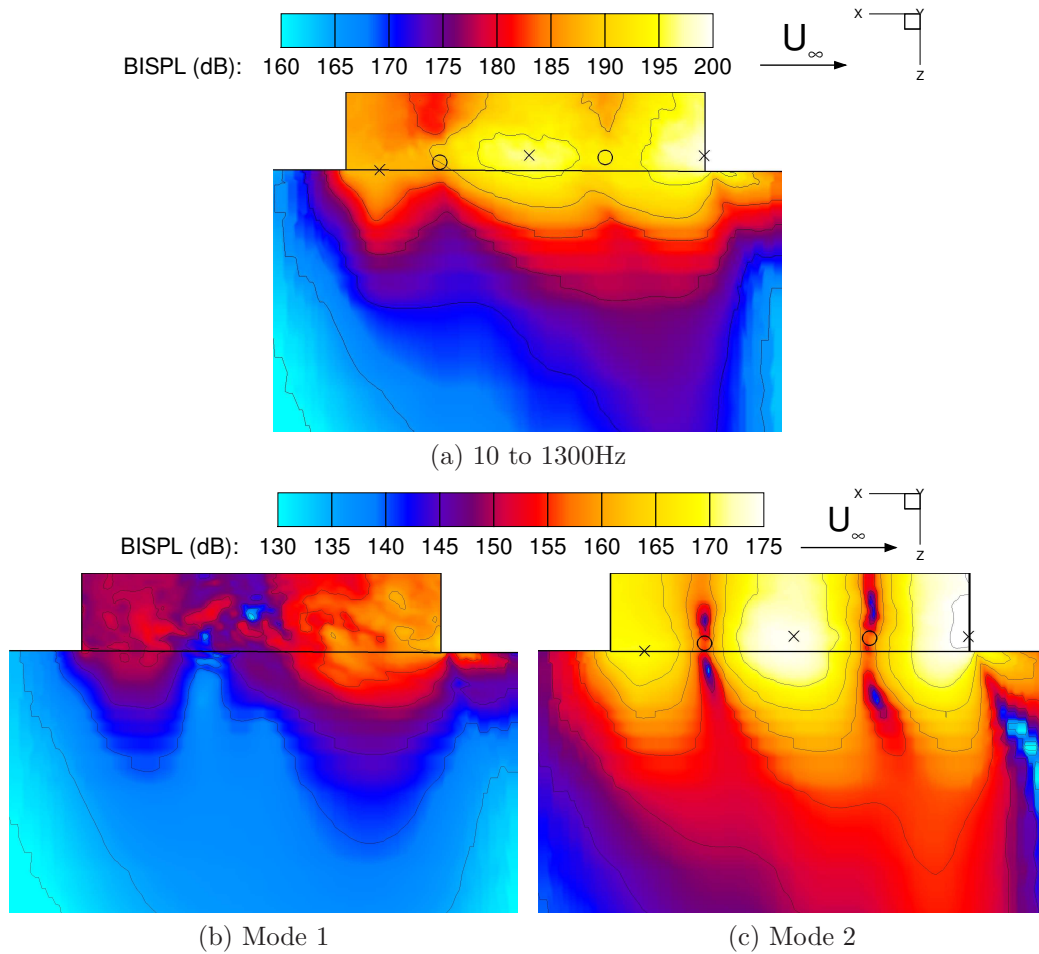
6   Beamforming Analysis

(a) 10 to 1300Hz

(b) Mode 1   (c) Mode 2

Figure 10: BISPL at the mid-span of the cavity over a large frequency band (a), and centred on the two first cavity modes in windows of 10Hz (b)-(c).

Using the full CFD flow-field of the M219 cavity with doors, the noise field

18

is computed and shown in figure 10 at the mid-span of the cavity. Between 10 and 1300Hz (Figure 10a), two main sources of noise are localised at the mid-length, and at the aft of the shear layer, due to the strong second cavity mode. The BISPL, is also integrated around cavity modes 1 and 2 in windows of 10Hz width (Figures 10b and 10c). All modes show alternatively high and low noise levels along the cavity length, corresponding to the nodes, and the antinodes of standing waves oscillations. The nodes of the dominant second mode are shown with circles, and the antinodes with crosses, in figures 10 to 14. The cavity modes are mainly produced along the shear layer, as seen by the peaks of the different modes close to the black line at Z=0.

(a) No flow-field

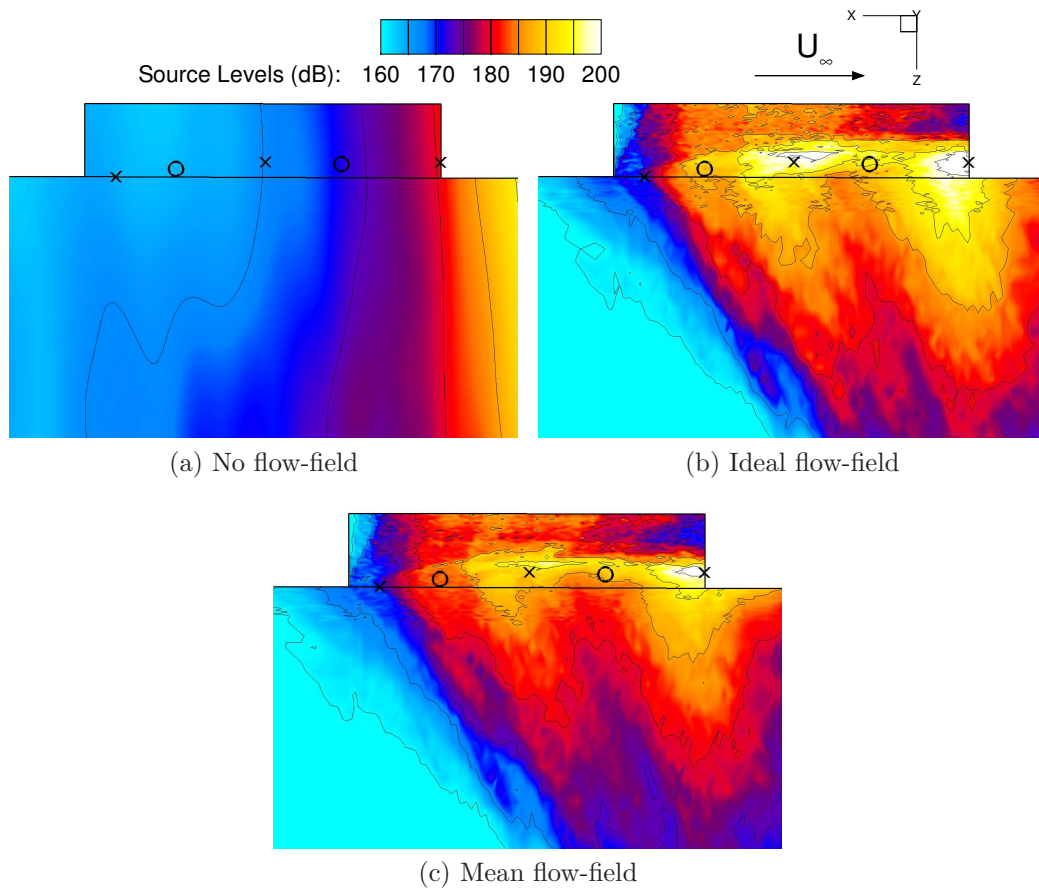(b) Ideal flow-field

(c) Mean flow-field

Figure 11: Noise reconstruction at the mid-span of the cavity over a large frequency band between 10 and 1300Hz for different noise propagation model. Multi-spiral array with 31 microphones, placed at Z/L=1.5.

19

Experiments are limited to probes placed on the wall, so they miss important characteristics of the noise field as described above. The beamforming is applied to the CFD results, with the objective to a obtain similar noise field compared to the BISPL computed with all the CFD points. The noise is reconstructed on a grid of 7290 points at the mid-span of the cavity. Figure 11 shows the effect of the level of accuracy of the flow-field used to transport the sound waves. The multi-spiral array with 31 microphones, placed at Z/L=1.5 is employed here. First, the pressure waves are assumed to travel along straight lines from the scanned points to the microphones in a zero velocity flowfield (Figure 11a). The noise is not correctly localised, with a peak downstream of the cavity. Assuming the pressure waves travelling in an ideal flowfield, (Figure 11b), with zero velocity in the cavity, and free-stream outside, the noise reconstruction is more accurate. The noise is localised around the shear layer, mainly at the second, and at the third antinodes of the second cavity mode (Second and third crosses in figure 11b). Nevertheless, the sources of noise are surrounded by large lobes along the vertical direction.

The best result is obtained using the CFD mean flow-field to transport the pressure waves (Figure 11c). The sources of noise are accurately localised at the shear layer, with a reduction of the lobe size. This is caused by the thickness of the shear layer, not taken into account by the ideal flow-field. The shape of the noise field bellow the cavity is also correctly reconstructed, with higher levels of noise at the second half of the cavity. The source of noise at the front of the cavity is weaker than the others, and is hidden by the lobes of the stronger noise sources. In the following, the mean flow is used for all beamforming results.

Figure 12 shows the influence of the vertical position of the multi-spiral array of 31 probes. The array closer to the cavity at Z/L=0.6 (Figure 12a), did not capture the sources at the shear layer, and the noise field close to the microphone array was not correctly reconstructed. Moving the array farther from the cavity, improves the reconstruction. The two main noise sources at 50%L and at 100%L of the shear layer are more visible, and the spread of the noise inside the cavity compares better with the BISPL. The near field influences the resulting reconstruction when the array is too close to the cavity, leading to errors [36].

Figure 13 shows the beamforming for the multi-spiral and the Dougherty arrays of 31 microphones, placed at 1.5%L from the cavity. The Dougherty design reconstruction did not capture the noise source at 50%L of the shear
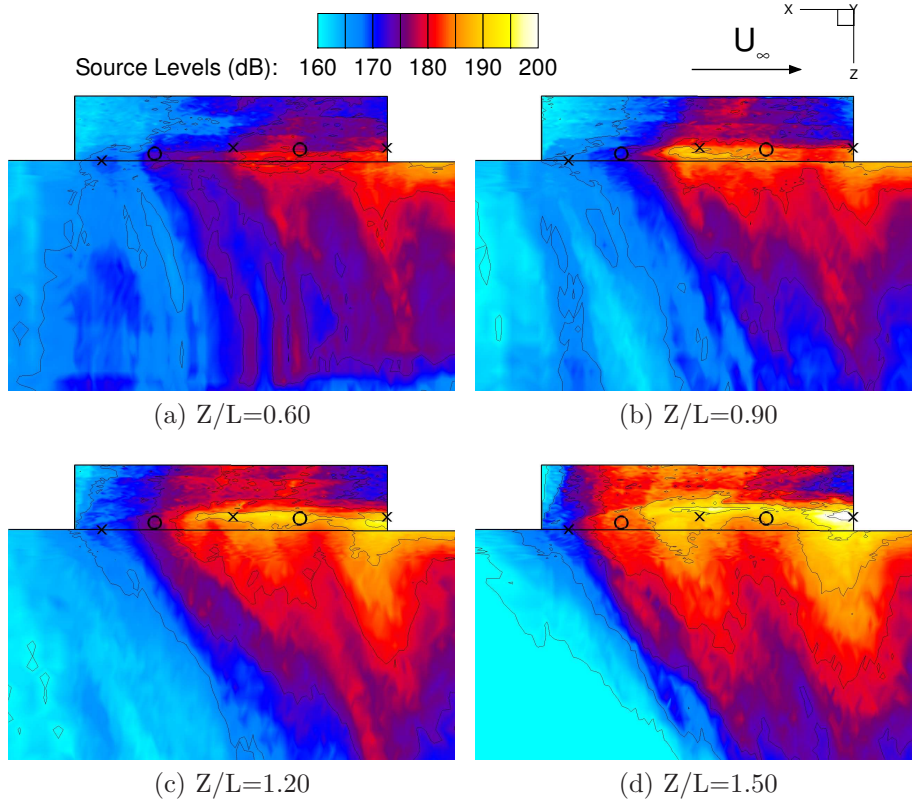
20

Figure 12: Noise reconstruction at the mid-span of the cavity over a large frequency band between 10 and 1300Hz for different multi-spiral array positions. Multi-spiral array with 31 microphones.

layer, and globally is less accurate than the multi-spiral array reconstruction. This may be the consequence of the lower density of microphones close to the perimeter of the Dougherty array, which reduces its bandwidth.

Figure 14 shows that the accuracy of the beamforming decreases with the number of microphones for the configurations tested. This may be caused by the strong broadband noise, that is amplified when summed over all microphones.

Figure 15 compares the BISPL and the beamforming for the M219 cavity without doors. Both the beamforming, and the BISPL, show the reduction of the noise source amplitude at the mid-length of the cavity, caused by a weaker second cavity mode without the doors.

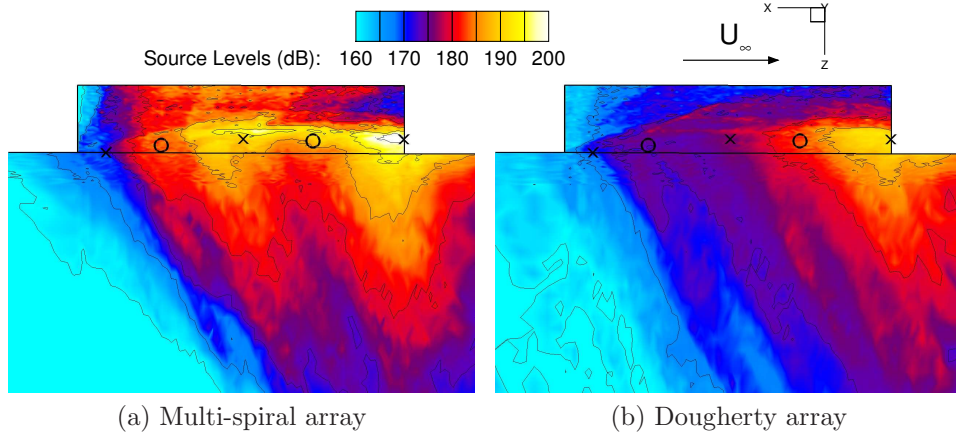This first attempt to apply the beamforming to cavity flows is encourag-

(a) Multi-spiral array   (b) Dougherty array

Figure 13: Noise reconstruction at the mid-span of the cavity over a frequency band between 10 and 1300Hz. Arrays of 31 microphones placed at Z/D=1.5.
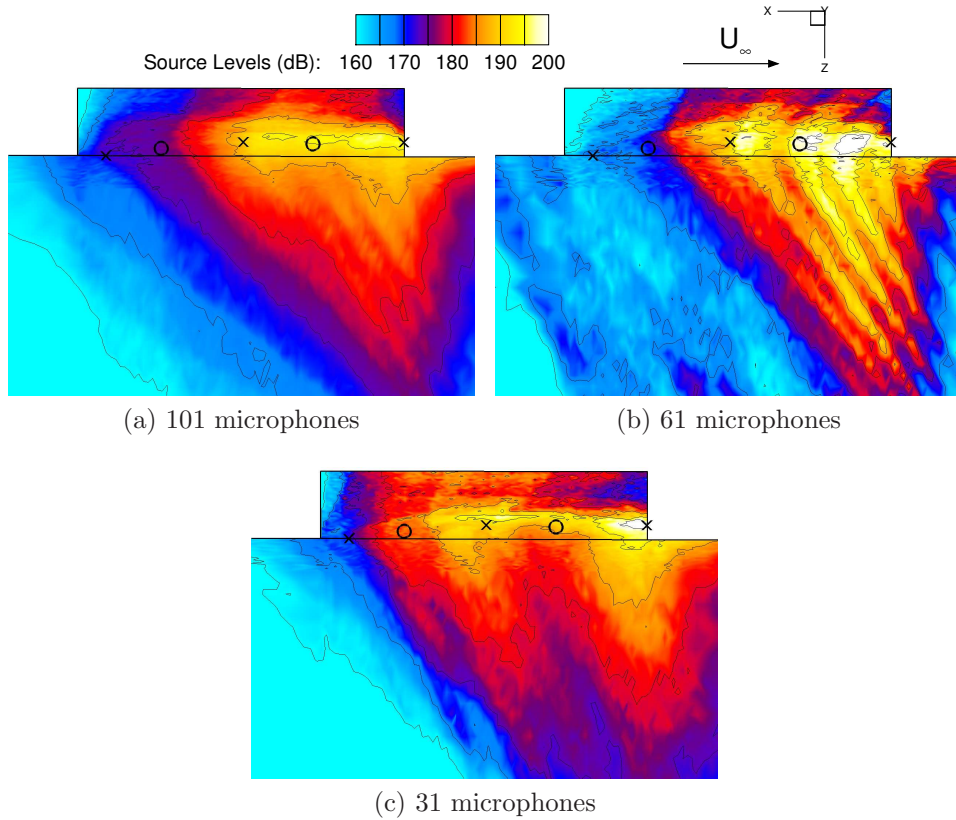

(a) 101 microphones   (b) 61 microphones

(c) 31 microphones

Figure 14: Noise reconstruction at the mid-span of the cavity over a frequency band between 10 and 1300Hz. Multi-spiral array placed at Z/L=1.5.
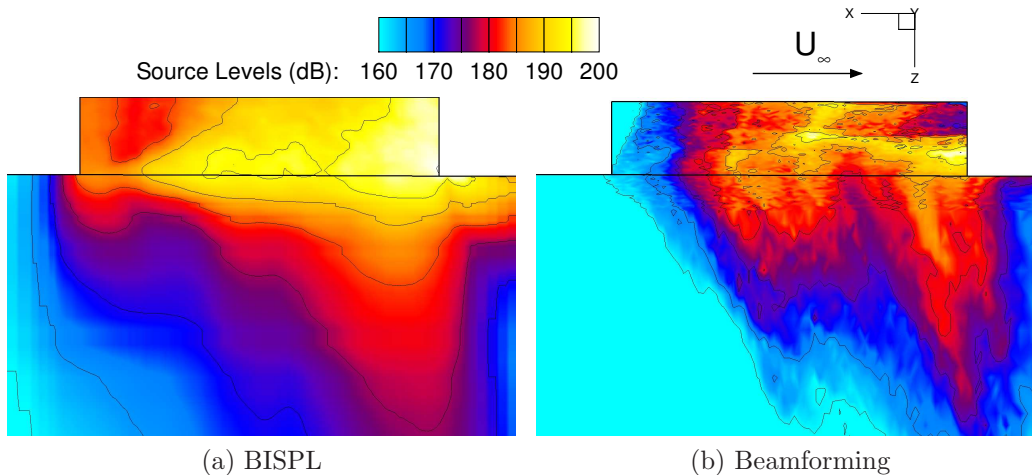
(a) BISPL · (b) Beamforming

Figure 15: Noise field at the mid-span of the M219 cavity without doors over a large frequency band between 10 and 1300Hz. Multi-spiral array of 31 microphones placed at Z/D=1.5.

ing, and suggests that if applied to wind tunnels, more physics could be seen in cavity flow.

6.1 Analysis of the Noise Generation Mechanism

The Rossiter cavity flow model [1] assumes an hydrodynamic interaction, between the periodic shedding of vortices travelling downstream at the shear layer convective speed of $\kappa_\nu U_\infty$, and the reflected acoustics waves travelling upstream at the speed of the sound c. κ_ν is the Rossiter's convective velocity.

Based on the observation of standing waves in cavity flows, and the presence of numerous reflected waves in experiments [37, 38, 39, 2], it is assumed that the main mechanism driving the tone generation is similar to a standing wave resonator. Other papers made this assumption as Casper *et al.*[40] considering one upstream wave travelling at the speed of sound c, and one downstream travelling wave travelling at $0.57U_\infty$. The simple model was able to reproduce the mode shape, but the flow dynamics was not in agreement with the experiments. The modulation of the tones, and their existence were not predicted. The simplest resonator in fluid dynamics is a pipe closed at both ends, where pressure waves $P_i(x,t)$ are alternatively reflected at each ends, and travel at the speed of the sound along the pipe. The superposi-
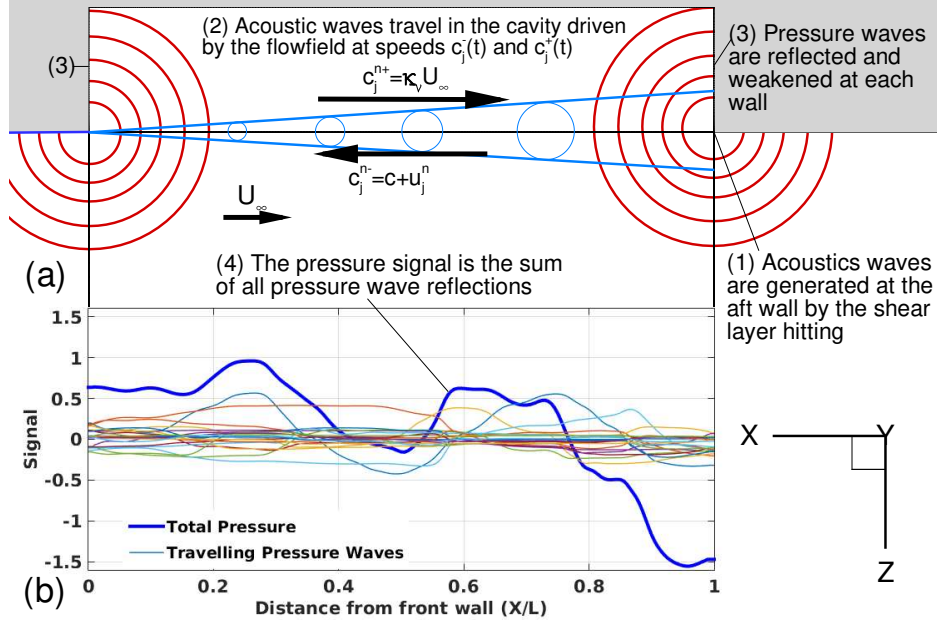
Figure 16: (a) Standing waves schematic, (b) Reflections and resulting pressures in cavity.

tion of the pressure waves leads to strong pressure fluctuations, of frequency defined by the pipe length.

In a similar fashion, the cavity resonance is represented by an one dimensional standing wave resonator, shown figure 16. The space is uniformly discretised in N_p points, and the pressure of the i-th reflected wave at a point j, and at the timestep n is noted as $P_{i,j}^n$. The front wall is localised at j=0, and the aft wall at $j = N_p$. First, the pressure waves are generated as the shear layer impact at the downstream corner (position (1) in figure 16), and this pressure is given by the sum:

$$P_{0,N_p}^n = \sum_{f=1}^{f_N} A_f sin(2\pi f t_n + 2\pi R_i) \qquad (17)$$

with f the wave frequency, f_N the frequency of the last wave, A_f the wave amplitude, R_i a random phase shift for each frequency, and t_n the time at the timestep n. In shallow cavity flows, the broadband noise amplitude A_f is decreasing with the frequency, and the modes are usually seen up to Rossiter mode 5 depending on the case. To produce a signal P_{0,N_p}^n representative of

24

a turbulent flow, the maximum pressure wave frequency f_N is set to a large value, here 3000Hz, and the wave amplitude A_f is linearly decreasing with the frequency:

$$A_f = A_0 \frac{f_N - f}{f_N} \tag{18}$$

As the amplitude of this signal depends on various parameters, including the Mach Number, or the thickness of the incoming shear layer, an arbitrary amplitude $A_0 = 26.5 Pa$ is set for the output to fit as best as possible the CFD results. The pressure waves travel towards the opposite wall ((2) in figure 16), and are alternatively reflected ((3) in figure 16) at the front, and at the aft walls, assuming an absorption by the reflection defined as:

$$P_{i+1,0}^{n+1} = R_w A_t P_{i,0}^n \quad \text{at the front corner} \tag{19}$$

$$P_{i+1,N_p}^{n+1} = R_w A_t P_{i,N_p}^n \quad \text{at the aft corner} \tag{20}$$

with R_w the reflection coefficient at the wall defined as [41]:

$$R_w = \frac{Z_{steel} - Z_{air}}{Z_{steel} + Z_{air}} = 0.98 \tag{21}$$

with respectively Z_{steel}, and Z_{air} the steel (for the cavity walls), and air acoustic impedance. A_t is an absorption coefficient, assuming losses during the pressure wave travelling due to the viscosity, the turbulent flow, and the acoustic damping. This coefficient is set to 0.95 here for the purposes of demonstrating the method.

The waves are numerically transported using an upwind scheme of third order [42]:

$$P_{i,j}^{n+1} = P_{i,j}^n - c_j^{n+1} \Delta t \frac{2P_{i,j+1}^n + 3P_{i,j}^n - 6P_{i,j-1}^n + P_{i,j-2}^n}{6\Delta x} \tag{22}$$

with Δx the grid spacing, Δt the timestep, and c_j^n the wave speed at the point j. The upstream, and downstream travelling waves move out of sync at velocities respectively defined as:

$$c_j^{n-} = c - u_j^n \quad \text{and} \quad c_j^{n+} = \kappa_\nu U_\infty \tag{23}$$

with c the sound speed, and u_j^n the axial flowfield velocity along the propagation path of the pressure waves. This formulation of c_j^{n+} follows from Rossiter who assumed that the downstream travelling pressure waves are transported by the shed vortices. The reflected pressure wave $P_{i,j}^n$ is removed

from the computation when its amplitude becomes weaker than 5% of P_{0,N_p}. Reducing this limit further does not influence the final result. Finally, the resulting pressure signal $P_{t,j}^n$ is the sum of all reflections (curve (4) in figure 16):

$$P_{t,j}^n = \sum_{i=1}^{N_r} P_{i,j}^n \qquad (24)$$

with N_r the number of reflections.

The analysis is applied to the M219 cavity without doors, with $\Delta x = 0.0025m$ and $\Delta t = 1.10^{-6}s$. Three different assumptions on the velocities c_j^{n+} and c_j^{n-} driving the pressure wave propagation are tested. Figure 17, the unsteady speeds are only presented for selected time steps. First, the ideal wave resonator models the pressure waves travelling through a medium with $c_j^{n+} = c_j^{n-} = c$, like a pipe closed at both ends. The sound pressure level in figure 18a shows an infinite number of linearly spaced tones following the formula:

$$f_m = \frac{m}{2L}c \qquad (25)$$

To reduce the tonal frequencies, the steady flow resonator considers pressure waves travelling at a reduced speed with respect to the mean stream-wise flow computed with CFD. The upstream travelling waves consider u_j^{n+} along a line in the shear layer at Y=0 and Z/L=-0.04, where the tonal noise is maximum, as shown in figure 10a. The downstream travelling waves travel along with the shed vortices at about 69% of the free-stream velocity. This value was chosen to fit as better as possible the experimental frequencies. The steady flow resonator improves the results (Figure 18b) with a better estimation of cavity tone frequencies, within 40Hz. However, an infinite number of tones are predicted, not in agreement with experiments.

The accuracy of the analysis is improved using the unsteady flow to drive the pressure wave propagation. The CFD signal of 30 travel times is looped to a length of 500 travel times. The upstream pressure waves propagate here with an unsteady velocity that is comprised between 0 and 400m/s. The sound pressure levels in figure 18c show better agreement between the analysis and the experiments. The unsteady flow resonator predicts a finite number of modes, and broadband noise for the higher frequencies. This highlight that the modal amplitudes are driven by the turbulence around the cavity.
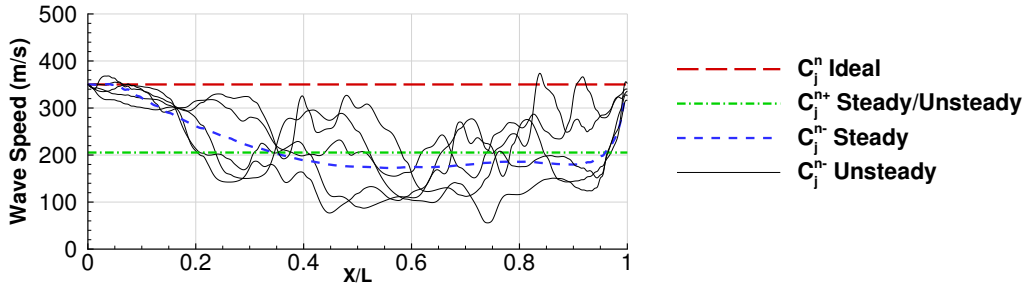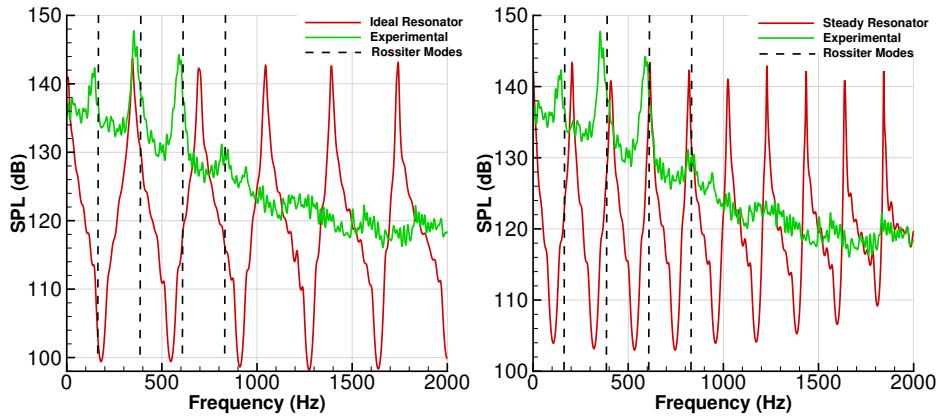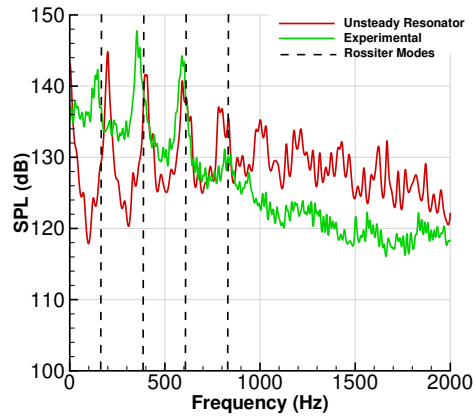
Figure 17: Pressure wave speed c_j^n along the cavity length.

(a) Ideal Resonator

(b) Steady Resonator

(c) Unsteady Resonator

Figure 18: SPL at the aft wall of the M219 cavity. L=0.51m.

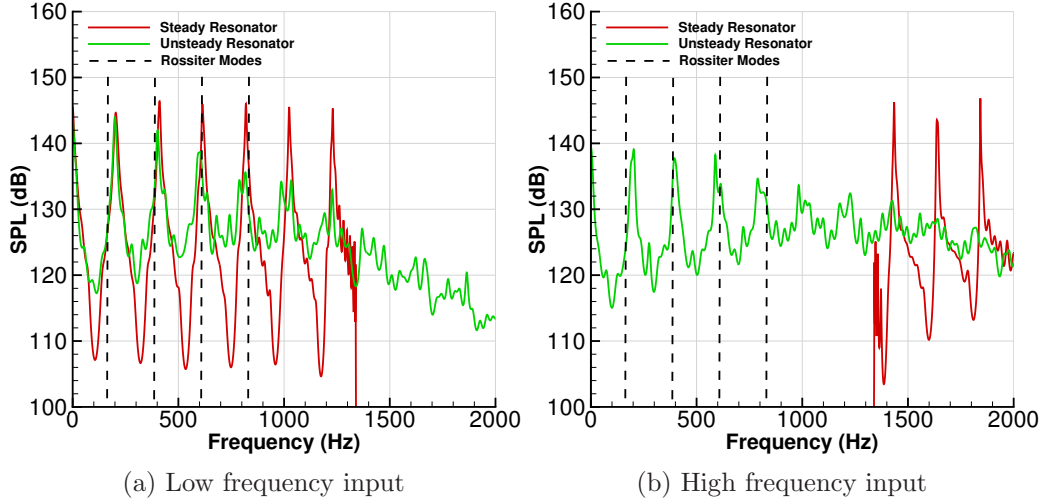(a) Low frequency input   (b) High frequency input

Figure 19: SPL at aft wall of the cavity for different input signals.

Figure 19, the steady and unsteady resonators are used with two different signal inputs. The low frequency signal contains wave lengths larger than half a cavity length, and the high frequency signal wave lengths smaller than this limit. This wave length is equivalent to a frequency f_L of 1370Hz for a cavity length of 0.51m. The steady resonator provides a similar output for both inputs, with peaks and broadband noise limited to the frequencies ranges of the input signal. However, the unsteady resonator generates a very different answer. With low frequency input (Figure 19a), the peaks are dumped from the third mode, and broadband noise appears above f_L. Employing the high frequency input, unexpected fluctuations arise (Figure 19b). The peaks above f_L are totally dumped in favor of broadband noise, and high amplitude peaks appear at the Rossiter mode frequencies. This suggests that the flowfield turbulence modifies the resonance mechanism, moving the energy from the high frequencies to the cavity modes. The high frequency resonance is disabled by the wave speed unsteadiness, that makes difficult for the upstream, and the downstream waves to be in phase, as their wavelengths are comparable, or smaller than the length scale of the flow fluctuations. This promotes broadband noise for high frequencies.

Figure 20 shows the output of the the unsteady resonator using the high frequency input. The wavelet transform is shown in function of the travel time at 95% of the cavity length. The energy leeks quickly to low frequencies,
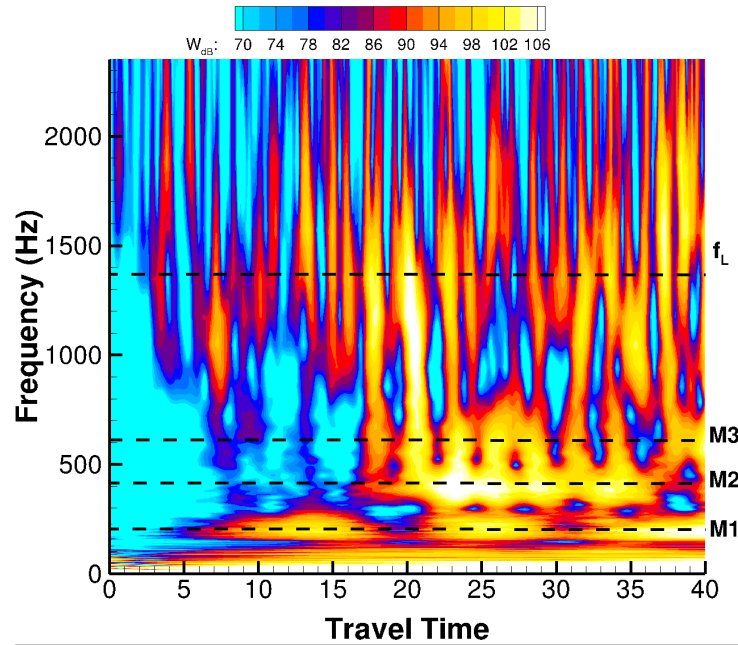
Figure 20: Scalogram at 95% of the cavity length. High frequency input applied to the unsteady resonator.

and after 5 travel times, the first cavity mode appears. The second and third modes appear after 17 travel times. The energy transfer from high to low frequencies may explains why cavity flow are so noisy, and fast to settle [43]. When the flow establishes, the shear layer hits the aft wall producing high frequency pressure waves reflecting inside the cavity. By superposition, this generates strong cavity modes at low frequencies due to the flowfield turbulence. Then, the cavity modes excite the shear layer motion that further amplify the low frequencies in the pressure waves produced at aft wall. This feedback loop further amplifies the resonance, and the cavity modes lock to their final frequencies.

The Banded Integral Wavelet (BIWs) are shown for modes 1 to 3 for the unsteady flow resonator and the experimental results along the ceiling mid-span (Figures 21). The scalogram is integrated in windows of 20Hz centred on the cavity modes. There is a good agreement of the unsteady resonator with the experiments, showing standing waves of similar shape.

The BIW envelope is shown figure 22. The unsteady resonator predicts the tonal amplitude modulation, and the mode shapes. As the analysis does
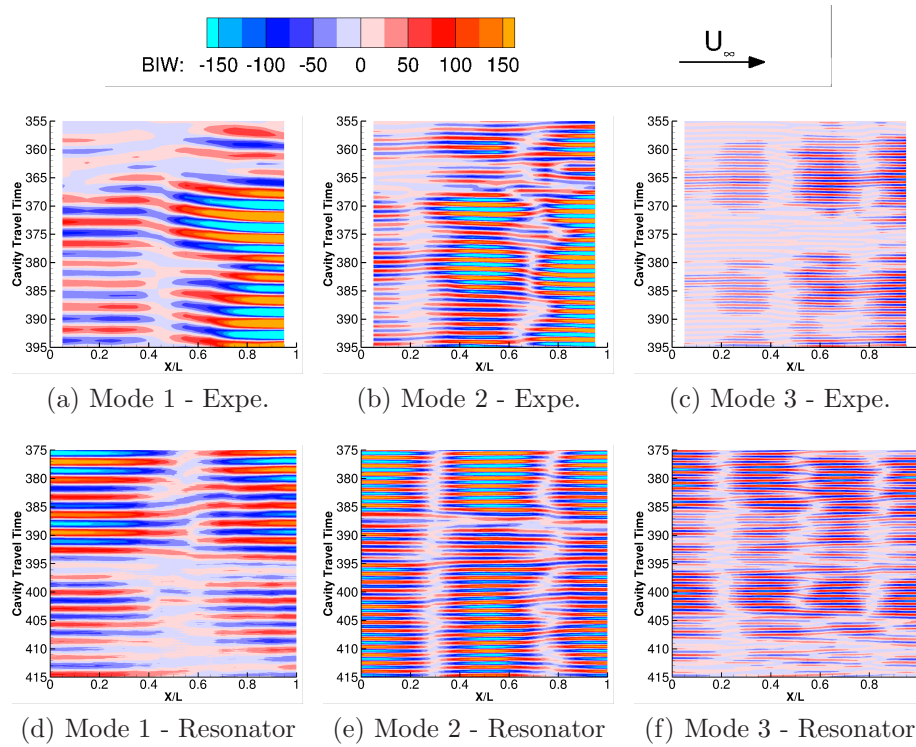
29

(a) Mode 1 - Expe. (b) Mode 2 - Expe. (c) Mode 3 - Expe.

(d) Mode 1 - Resonator (e) Mode 2 - Resonator (f) Mode 3 - Resonator

Figure 21: BIW at ceiling mid-span for experimental and unsteady resonator.

(a) Mode 1 - Expe. (b) Mode 2 - Expe. (c) Mode 3 - Expe.

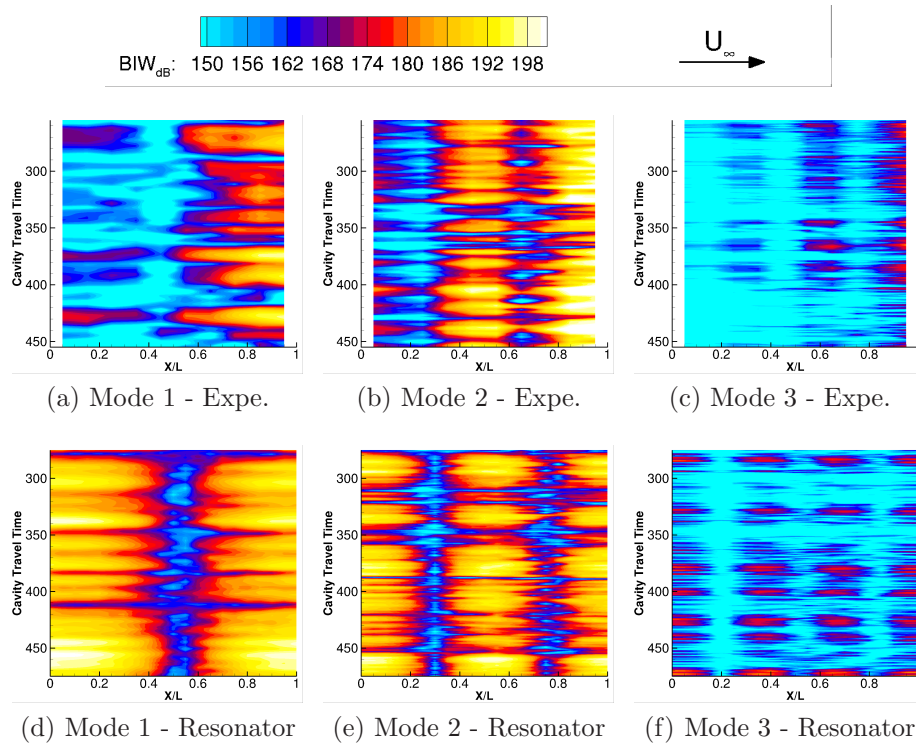(d) Mode 1 - Resonator (e) Mode 2 - Resonator (f) Mode 3 - Resonator

Figure 22: BIW envelope at ceiling mid-span for experimental and unsteady resonator.

30

not include the noise fluctuations associated to the shear layer turbulence, and the noise radiating from all cavity surfaces, the gradient of noise between the front and the aft of the cavity is not well captured.

Figure 23 shows the spectrum of the cavity tonal amplitude modulation (BIW envelope) at 95% of the cavity length for modes 1 to 4. The experimental signal is characterised by decreasing modulation amplitude with the frequency. The first mode modulation has a peak at a very small frequency as shown by Kegerise *et al.*[9] (Vertical dashed line in figure 23a). The steady resonator fails to fit the experiments with under-prediction of the low fre-
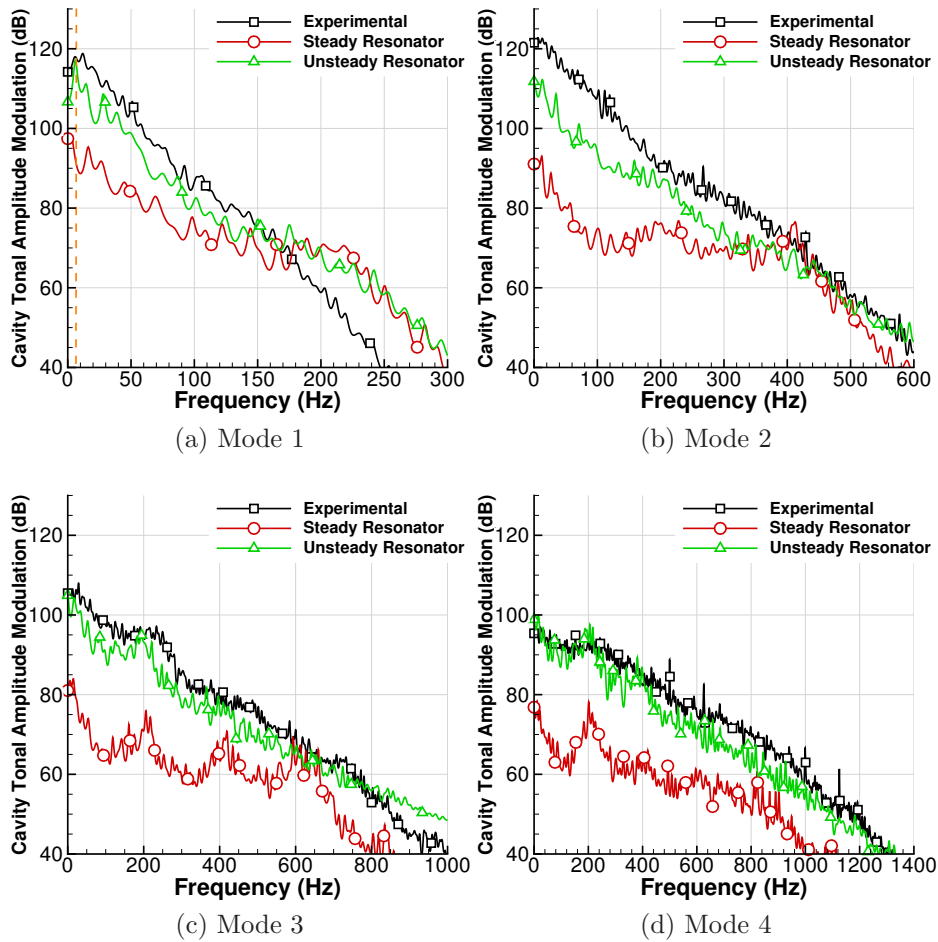

(a) Mode 1 (b) Mode 2

(c) Mode 3 (d) Mode 4

Figure 23: Tonal amplitude modulation at X/L=0.95.

quencies. On the other hand, the unsteady resonator agrees well for the modes 1, 3 and 4, while the mode 2 modulation is only slightly underestimated. The third mode modulation shows peaks at 200, 400 and 600Hz, and the fourth mode at 200Hz. Those peaks are dumped by the unsteadiness of the flowfield in favor of broadband noise.

This analysis gives an accurate picture of the transonic cavity flow dynamics, showing that the wave superposition is the main physics driving the cavity flow. However, it must be noticed that the relative modal amplitudes are not exactly represented here compared to the experiments, highlighting a missing part of the physics. In future work, the pumping action at the aft wall will be taken into account. The tonal pressure fluctuations and the shear layer motion[2] have to be coupled to generate the pressure at aft wall P_{0,N_p} regarding the pressure history.

7 Conclusions

The aim of this work is to improve the understanding of the physical mechanisms driving transonic cavity flows.

CFD solutions have to be accurate in terms of mean, and unsteady values of the flowfield. Joint space-time analysis, using wavelet transform, provided a meaningful validation for the unsteady part of the cavity flows. The tonal fluctuations, including the standing waves, and the tonal amplitude modulation, were in fair agreement between Scale Adaptive Simulation [20] and experiments.

The understanding of cavity flows also relies on experiments where it is difficult to measure the flowfield far from the walls. The beamforming was able to capture the noise field around the cavity using a limited number of probes. The mean CFD flow-field has to be provided to compute the propagation of the noise. This technique could be used in wind tunnel, coupling a microphone array measurement, and the PIV techniques. The benefit of the beamforming will be important for complex cavity configurations, with various noise sources, and noise propagation paths.

The cavity dynamics were modelled as a standing wave resonator, influenced by the shear layer flow. This study suggests that the generation mechanism of cavity noise proposed by Rossiter can be complemented with the superposition of the pressure waves reflecting, and travelling inside the bay. The time averaged flow-field drives the tonal frequencies, while the flow-field

fluctuations drive their amplitude, and feed the broadband noise. More importantly, the turbulence feeds the Rossiter modes with energy coming from higher frequencies. This may be the trigger of the cavity flow resonance. For the first time, the tonal dynamics of the cavity flow are fully represented by a model with the standing wave-like oscillations and their modulation. This explains why past cavity flows models considering a small number of pressure reflections were not able to capture the cavity dynamics.

To go farther, the analysis will have to account for the motion of the shear layer induced by the tonal pressure fluctuations, that influences the pressure waves generated at the aft wall.

References

[1] Rossiter, J. E., "Wind Tunnel Experiments on the Flow Over Rectangular Cavities at Subsonic and Transonic Speeds," Technical Report 64037, Royal Aircraft Establishment, Bedford, UK, October 1964.

[2] Schmit, R., Grove, J., Semmelmayer, F., and Haverkamp, M., "Nonlinear feedback mechanisms inside a rectangular cavity," *AIAA Journal*, Vol. 52, No. 10, 2014, pp. 2127 – 2142, doi:10.2514/1.J052804.

[3] Lawson, S. and Barakos, G., "Review of Numerical Simulations For High-Speed, Turbulent Cavity Flows," *Progress in Aerospace Sciences*, Vol. 47, No. 3, 2011, pp. 186 – 216, doi:10.1016/j.paerosci.2010.11.002.

[4] Tam, C. and Block, P., "On the tones and pressure oscillations induced by flow over rectangular cavities," *Journal of Fluid Mechanics*, Vol. 89, No. 2, 1978, pp. 373–399, doi:10.1017/S0022112078002657.

[5] Handa, T., Miyachi, H., Kakuno, H., Ozaki, T., and Maruyama, S., "Modeling of a feedback mechanism in supersonic deep-cavity flows," *AIAA Journal*, Vol. 53, No. 2, 2015, pp. 420–425, doi:10.2514/1.J053184.

[6] Alvarez, J., Kerschen, E., and Tumin, A., "A theoretical model for cavity acoustic resonances in subsonic flow," *Proceedings of the 10th AIAACEAS Aeroacoustics Conference*, Paper No. AIAA 2004-2845, Manchester, UK, 2004, doi:10.2514/6.2004-2845.

[7] Heller, H., Holmes, D., and Covert, E., "Flow-Induced Pressure Oscillations In Shallow Cavities," *Journal of Sound and Vibration*, Vol. 18, No. 4, 1971, pp. 545 – 553, doi:10.1016/0022-460X(71)90105-2.

[8] Wagner, J., Casper, K., Beresh, S., Arunajatesan, S., Henfling, J., Spillers, R., and Pruett, B., "Relationship between acoustic tones and flow structure in transonic cavity flow," *Proceedings of the 45th AIAA Fluid Dynamics Conference, AIAA AVIATION Forum*, Paper No. AIAA 2015-2937, American Institute of Aeronautics and Astronautics Inc, Dallas, TX, United States, 2015, doi:10.2514/6.2015-2937.

[9] Kegerise, M. A., Spina, E. F., Garg, S., and III, L. N. C., "Mode-switching and nonlinear effects in compressible flow over a cavity," *Physics of Fluids*, Vol. 16, No. 3, 2004, pp. 678–687, doi:10.1063/1.1643736.

[10] Flaherty, W., Reedy, T., Elliott, G., Austin, J., Schmit, R., and Crafton, J., "Investigation of cavity flow using fast-response pressure-sensitive paint," *AIAA Journal*, Vol. 52, No. 11, 2014, pp. 2462–2470, doi:10.2514/1.J052864.

[11] Lawson, S. J., Steijl, R., Woodgate, M., and Barakos, G. N., "High performance computing for challenging problems in computational fluid dynamics," *Progress in Aerospace Sciences*, Vol. 52, No. 1, 2012, pp. 19–29, doi: 10.1016/j.paerosci.2012.03.004.

[12] Hirt, C. W., Amsten, A. A., and Cook, J. L., "An Arbitrary Lagrangian-Eulerian Computing Method for All Flow Speeds," *Journal of Computational Physics*, Vol. 14, No. 3, 1974, pp. 227–253, doi: 10.1006/jcph.1997.5702.

[13] Osher, S. and Chakravarthy, S., "Upwind Schemes and Boundary Conditions with Applications to Euler Equations in General Geometries," *Journal of Computational Physics*, Vol. 50, No. 3, 1983, pp. 447–481, doi:10.1016/0021-9991(83)90106-7.

[14] Roe, P., "Approximate Riemann Solvers, Parameter Vectors and Difference Schemes," *Journal of Computational Physics*, Vol. 43, No. 2, 1981, pp. 357–372, doi:10.1016/0021-9991(81)90128-5.

[15] van Leer, B., "Towards the ultimate conservative difference scheme. V.A second-order sequel to Godunov's Method," *Journal of Computational Physics*, Vol. 32, No. 1, 1979, pp. 101–136, doi:10.1016/0021-9991(79)90145-1.

[16] van Albada, G., van Leer, B., and Roberts, W., *A Comparative Study of Computational Methods in Cosmic Gas Dynamics*, *Upwind and High-Resolution Schemes*, edited by M. Y. Hussaini, B. van Leer, and J. Van Rosendale, Springer Berlin Heidelberg, Berlin, Heidelberg. Germany, 1997, pp. 95–103, doi:10.1007/978-3-642-60543-7_6.

[17] Axelsson, O., *Iterative Solution Methods*, Cambridge University Press, Cambridge, MA, United States, 1994, pp. 504–557, doi:10.1017/CBO9780511624100.

[18] Jameson, A., Schmidt, W., and Turkel, E., "Numerical Solutions of Euler Equations by Finite Volume Methods Using Runge-Kutta Time-Stepping Schemes," *Proceedings of the Fourteenth Fluid and Plasma Dynamic Conference*, Paper No. 1981-1259, American Institute of Aeronautics and Astronautics Inc, Palo Alto, CA, United States, 1981, pp. 1–19, doi:10.2514/6.1981-1259.

[19] Jarkowski, M., Woodgate, M., Barakos, G., and Rokicki, J., "Towards Consistent Hybrid Overset Mesh Methods for Rotorcraft CFD," *International Journal for Numerical Methods in Fluids*, Vol. 74, No. 8, 2014, pp. 543–576, doi:10.1002/fld.3861.

[20] Menter, F. and Egorov, Y., "The Scale-Adaptive Simulation Method for Unsteady Turbulent Flow Predictions. Part 1: Theory and Model Description," *Flow, Turbulence and Combustion*, Vol. 85, No. 1, 2010, pp. 113–138, doi:10.1007/s10494-010-9264-5.

[21] Egorov, Y., Menter, F., Lechner, R., and Cokljat, D., "The Scale-Adaptive Simulation Method for Unsteady Turbulent Flow Predictions. Part 2: Application to Complex Flows," *Flow, Turbulence and Combustion*, Vol. 85, No. 1, 2010, pp. 139–165, doi:10.1007/s10494-010-9265-4.

[22] Babu, S., Zografakis, G., Barakos, G. N., and Kusyumov, A., "Evaluation of scale-adaptive simulation for transonic cavity flows." *International Journal of Engineering Systems Modelling and Simulation*, Vol. 8, No. 2, 2016, pp. 106–124, doi:10.1504/IJESMS.2016.075510.

[23] Childers, D., *Modern Spectrum Analysis*, Chapter 2, pp. 23-148. IEEE Press, New York, 1978.

[24] Larcheveque, L., Sagaut, P., and Comte, P., "Large-Eddy Simulation of a Compressible Flow in a Three-Dimensional Open Cavity at High Reynolds Number," *Journal of Fluid Mechanics*, Vol. 516, 2004, pp. 265–301, doi:10.1017/S0022112004000709.

[25] Pierce, A., *Acoustics: An Introduction to its Physical Principles and Applications*, Woodbury, New York: Acoustical Society of America, 1989.

[26] Bussow, R., "An algorithm for the continuous Morlet wavelet transform," *Mechanical Systems and Signal Processing*, Vol. 21, No. 8, 2007, pp. 2970–2979, doi:10.1016/j.ymssp.2007.06.001.

[27] Schmidt, R. O., "Multiple Emitter Location and Signal Parameter." *IEEE Transactions on Antennas and Propagation*, Vol. AP-34, No. 3, 1986, pp. 276–280, doi:10.1109/TAP.1986.1143830.

[28] Simley, E., *Developement of an Acoustic Array for Wind Turbine Aeroacoustic Noise Analysis.*, Ph.D. thesis, University of Colorado, April 2010.

[29] Nightingale, D., Ross, J., and Foster, G., "Cavity Unsteady pressure measurements - Examples from Wind-Tunnel Tests," Tech. Rep. Version 3, Aerodynamics & Aeromechanics Systems Group, QinetiQ, Bedford, UK, November 2005.

[30] Prime, Z. and Doolan, C., "A comparison of popular beamforming arrays," *Proceedings of the Annual Conference of the Australian Acoustical Society 2013*, Australian Acoustical Society, Victor Harbor, SA, Australia, 2013, pp. 151–157.

[31] Lee, B., "Effect of Captive Stores on Internal Weapons Bay Floor Pressure Distributions," *Journal of Aircraft*, Vol. 47, No. 2, March-April 2010, pp. 732–735, doi:10.2514/1.46684.

[32] Allen, R., Mendona, F., and Kirkham, D., "RANS and DES turbulence model predictions of noise on the M219 cavity at M=0.85," *International Journal of Aeroacoustics*, Vol. 4, No. 1, 2015, pp. 135–151, doi:10.1260/1475472053730039.

[33] Peng, S.-H., *M219 Cavity Flow*, *DESider A European Effort on Hybrid RANS-LES Modelling*, edited by W. Haase, M. Braza, and A. Revell, Vol. 103, Springer International Publishing, 2009, pp. 270–285, doi:10.1007/978-3-540-92773-0.

[34] Temmerman, L., Tartinville, B., and Hirsch, C., *URANS Investigation of the Transonic M219 Cavity*, *Progress in Hybrid RANS-LES Modelling: Papers Contributed to the 4th Symposium on Hybrid RANS-LES Methods, Beijing, China, September 2011*, edited by S. Fu, W. Haase, S.-H. Peng, and D. Schwamborn, Springer Berlin Heidelberg, Berlin, Heidelberg, 2012, pp. 471–481, doi:10.1007/978-3-642-31818-4_41.

[35] Ross, J. A., "PIV Measurements of the flowfields in an Aerodynamically Deep Cavity," Tech. rep., Aerodynamics & Aeromechanics Systems Group, QinetiQ, Bedford, UK, October 2002.

[36] Ryan, J. G., "Criterion for the minimum source distance at which plane-wave beamforming can be applied," *The Journal of the Acoustical Society of America*, Vol. 104, No. 1, 1998, pp. 595–598, doi:10.1121/1.423289.

[37] Heller, H. and Bliss, D., "The physical mechanism of flow-induced pressure fluctuations in cavities and concepts for their suppression," *Proceedings of the 2nd Aeroacoustics Conference*, Paper No. AlAA 1975-491, Hampton, VA, United States, 1975, doi:10.2514/6.1975-491.

[38] Kegerise, M., Spina, E., and Cattafesta, L., "An experimental investigation of flow-induced cavity oscillations," *Proceedings of the 30th Fluid Dynamics Conference*, Paper No. AlAA 99-3705, Norfolk,VA, United States, 1999, doi:10.2514/6.1999-3705.

[39] Garg, S. and Cattafesta III, L., "Quantitative schlieren measurements of coherent structures in a cavity shear layer," *Experiments in Fluids*, Vol. 30, No. 2, 2001, pp. 123–134, doi:10.1007/s003480000147.

[40] Casper, K., Wagner, J., Beresh, S., Spillers, R., Henfling, J., and Dechant, L., "Spatial distribution of pressure resonance in compressible cavity flow," *Proceedings of the 55th AIAA Aerospace Sciences Meeting*, Paper No. AIAA 2017-1476, Grapevine, TX, United States, 2017, doi:10.2514/6.2017-1476.

[41] Lurton, X., *An Introduction to Underwater Acoustics: Principles and Applications*, Praxis Publishing, 1st ed., 2002, p. 63.

[42] Hirsch, C., *Numerical Computation of Internal and External Flows: The Fundamentals of Computational Fluid Dynamics*, Butterworth-Heinemann, 2nd ed., 1980, p. 197.

[43] Loupy, G., Barakos, G., and Taylor, N., "Cavity Flow Over a Transonic Weapon Bay During Door Operation," *Journal of Aircraft*, 2017, Accepted for publication.